

Article

# Effect of Lateral End Plates on Flow Crossing a Yawed Circular Cylinder

Hui Liang and Ri-Qiang Duan \* 

Institute of Nuclear and New Energy Technology, Collaborative Innovation Center of Advanced Nuclear Energy Technology, Key Laboratory of Advanced Reactor Engineering and Safety of Ministry of Education, Tsinghua University, Beijing 100084, China; tokaimura2009@gmail.com

\* Correspondence: duanrq@tsinghua.edu.cn

Received: 12 March 2019; Accepted: 15 April 2019; Published: 17 April 2019



**Featured Application:** Structure design of heat exchanger; wind effect of the building structure.

**Abstract:** Numerical simulation is carried out to investigate the effect of the boundary condition of two lateral end-plate walls on the flow structure in the wake of a flow crossing a yawed circular cylinder. Two typical boundary conditions, nonslip and periodic, are investigated. It is revealed that the boundary condition of the two end-plates has a significant effect on the flow behaviors in the wake. Under the nonslip boundary condition, the vortex structure in the wake exhibits a tapering shape to the tip end. The flow pattern is formed in the wake as the streamlines on the tip side are becoming denser while the streamlines on the base end are becoming sparser. Spectral power analysis of the local lift coefficient shows that the frequency distribution exhibits axial variation. On the base side, the frequency distribution is broadband. On the tip side, there are two peak frequencies: the larger one corresponds to the value predicted by the independence principle, and the smaller one is generated by the secondary axial flow separation from the rear cylinder wall. Under the periodic condition, the numerical results show that organized Strouhal vortex is shed in the wake in the same way as to the flow orthogonally passing a cylinder and the independence principle is still applicable.

**Keywords:** vortex shedding; secondary axial wall-attached flow; yaw angle; circular cylinder; LES

## 1. Introduction

Flow crossing a yawed circular cylinder is a significant issue, not only in academia but also from a practical point of view. In mechanical engineering, the induced vibration caused by crossing flow over heat transfer tubes has a severe impact on the mechanical integrity and life span of heat exchangers. In engineering applications, the so-called “independence principle” (proposed by Hoerner [1], hereinafter IP) is commonly used to evaluate the vortex shedding frequency of a uniform incoming flow crossing a yawed cylinder, assuming independence between the normal component and the axial component of the incoming flow velocity. In the IP hypothesis, a uniform flow passing a yawed cylinder is postulated as being quasi-two-dimensional, and the characteristics of the vortex wakes behind a circular cylinder are barely controlled by the normal component of the incoming flow velocity, such as organized Strouhal vortices shedding and vortex structure in the wake.

However, a literature review reveals that the validity of the IP is still in question. Conflicting conclusions on the IP validity for uniform flows crossing yawed circular cylinders have been made in previous reports. Earlier in 1982, Selby [2] experimentally investigated the applicability of the IP to subsonic turbulent flow over a swept rearward-facing step. It was shown that the validity of the IP is strongly dependent on the yaw angle, which is valid up to a yaw angle of 38 degrees. Hayashi et al. [3] measured in a wind tunnel the pressure distribution on the surface of a yawed circular cylinder and

investigated the wake size behind the yawed cylinder by a visualization technique. He concluded that a flow around a yawed circular cylinder is three-dimensional and nonuniform along the axis of the cylinder so that the IP is absolutely prevented. Moreover, they attributed the failure of the IP to the aspect ratio of the circular cylinder, which was very important for the flow characteristics related to vortex shedding. Zhao et al. [4] investigated three-dimensional flow past a yawed circular cylinder of infinite length using direct numerical simulation, in which the yaw angle changes from 0 to 60 degrees. It was concluded that the Strouhal number and mean drag coefficient agree well with the IP at different yaw angles. Hogan et al. [5] investigated the spanwise dependence of vortex-shedding from yawed circular cylinders. They concluded that the IP was shown to predict the vortex-shedding frequency reasonably well along the entire cylinder span for smaller yaw angles (less than 20 degrees), while the vortex-shedding in the wake becomes more disorderly. Zeinoddini et al. [6] experimentally investigated the validity of the IP for cross-flow passing a yawed cylinder. It was reported that the IP is to some degree valid at low inclination angles, but the peak lift force was noticeably different from the prediction of the IP. They ascribed the inconsistency to the neglect of the effects of the axial component of the flow in the IP hypothesis. Pierson et al. [7] numerically explored the flow past a yawed cylinder of finite length using the finite volume/fictitious domain method. They argued that the IP is inaccurate in the flow regime.

Therefore, there is significant uncertainty in basic characteristics such as vortex shedding in the wake as a flow crosses a yawed circular cylinder. Theoretically, the IP is based on the assumption that the Reynolds stress terms in the streamwise and spanwise equations are independent, which are only established for a yawed cylinder with an infinite length; otherwise, the IP solution is precluded. Therefore, the end conditions of a yawed cylinder are decisive factors for the vortex-shedding behavior in the wake as a flow sweeps it. The Ramberg experiments [8] have shown that the characteristics of the vortex wake behind yawed cylinders are very sensitive to the end conditions. Matsumoto [9] reviewed the various types of vortex generation and the related response characteristics of yawed cylinders. He found that on the flow crossing a yawed cylinder, besides alternate Karman vortex shedding, symmetrical vortex shedding, and axial vortex should also be taken into consideration. Furthermore, Matsumoto et al. [10] used a wind tunnel to investigate the mechanisms of vortex-induced vibration of inclined cables subjected to oblique cross-flow. It was revealed that the three-dimensional characteristics of vortex shedding are strongly dependent on the end conditions and the yaw angle of the cable. Matsumoto et al. [11] tried to clarify the details of the effect of axial flow, which flows in the near wake along the cylinder axis as the flow is inclined to cross the cylinder. However, they thought that their mechanisms are not sufficiently clear and should be further clarified. Thus, it is necessary to clarify the end effects and moreover provide quantified and sufficient analysis of the influence of the end effects. Hitherto, there are no specific studies on the thorough investigation of the effect of the end plates fitted with a yawed cylinder on the flow behavior in the wake. In this paper, we will strive to resolve this and fill the gap.

The boundary condition on the two lateral endplate walls can be generalized as two types. One is nonslip condition, which is commonly encountered in most practical engineering and natural phenomenon, e.g., flow crossing tubes in heat exchangers, wind sweeping strands pulling support of bridges, wind crossing poles supporting electricity-carrying cables, and wind crossing plant stalk and tree trunk. Another is a periodic condition, which is a simplified approximation of a cylinder with a large aspect ratio, e.g., sea stream passing undersea cables. The objectives of this paper are to investigate the effect of the boundary condition of two end-plate walls on the crossflow of a cylinder with a yaw angle. Considering that the crossflow component of velocity over a cylinder should dominate over the in-line component of velocity, the yaw angle in this research is chosen to be not greater than  $45^\circ$ . In the following calculation, three yaw angles are investigated respectively:  $15^\circ$ ,  $30^\circ$ , and  $45^\circ$ , corresponding to small, medium, and large yaw angle. The Reynolds number is set to 3900 for all calculations in this research. This Reynolds number is selected based on the following considerations. First, flow in the wake at this Reynolds number is fully turbulent according to previous

studies. Second, it has been shown that the sensitivity of hydrodynamic forces to the Reynolds number begins to be weak at this value [12].

## 2. Computational Methodology

The dimensionless transient equations of continuity and momentum for 3D incompressible flow of a Newtonian fluid are presented as follows [13]:

$$\nabla \cdot u = 0 \tag{1}$$

$$\frac{Du}{Dt} = -\nabla p + \frac{1}{Re} \nabla^2 u \tag{2}$$

where the dimensionless variables are expressed as

$$p = \frac{\bar{p}}{\rho U_0^2}, \quad x = \frac{\bar{x}}{D}, \quad t = \frac{\bar{t} U_0}{D}, \quad u = \frac{\bar{u}}{U_0} \tag{3}$$

The calculation configuration for flow crossing a yawed cylinder is built up with  $35 D \times n D \times 20 D$  in three dimensions, as shown in Figure 1a. The width of the calculation domain is taken as  $n D = 9 \times D$  for the nonslip wall boundary condition and  $n D = 6 \times D$  for the periodic wall boundary condition in order to save computational resource, which is enough to capture the feature of the wake flow for the periodic wall boundary condition. Two coordinate systems are defined, as shown in Figure 1b. One is the global coordinate system of  $Oxyz$ , in which the origin is located at the center of the midspan cross section of the cylinder, and the  $x$ -,  $y$ - and  $z$ -directions are defined respectively as the streamwise direction, the vertical direction, and the spanwise direction. The other is a cylinder-oriented coordinate system  $Ox'y'z'$ , in which the origin is overlapped with that of the global coordinate system, and the  $x'$ -,  $y'$ - and  $z'$ -directions are defined as the direction of the normal to the frontal stagnant edge, the same direction as  $y$ -, and the axial direction aligned with the cylinder axis. The yaw angle  $\alpha$  is defined as an angle between the normal to the cylinder  $x'$  and the incoming flow direction  $x$ , where  $\alpha = 0^\circ$  represents orthogonal cross-flow of a cylinder. A cylinder is clamped between two lateral end-plates. Its upstream end is attached with a base end-plate, and its downstream end is attached with a tip end-plate. The two vertical constraints of the domain are respectively named as ceiling and floor. The boundary conditions for the governing equations are set as follows. In the following simulation, our calculations are developed on the platform of the open source CFD software OpenFOAM®.

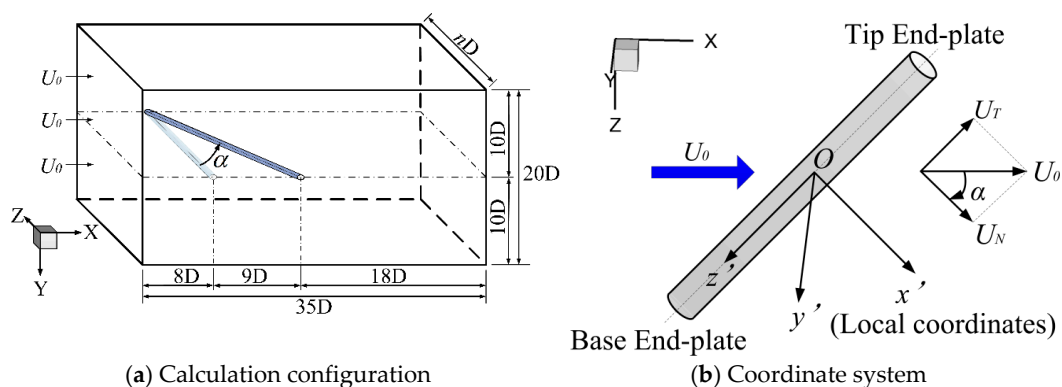


Figure 1. Definition of calculation configuration and coordinate system.

A uniform velocity is used to define the inlet condition, where the streamwise velocity component is set to a free uniform stream velocity  $U_0$  while the spanwise and vertical velocity components are set to zero. A Neumann boundary condition of pressure is imposed on the outlet with enough downstream length (18 times the diameter of the cylinder) to assure no backward flow on the outlet. The free-slip boundary condition is set on the ceiling and floor. The no-slip boundary condition is applied on the

cylinder wall. On the two lateral end-plate walls, both nonslip and periodic boundary conditions are used to investigate the effect on the flow characteristics in the wake.

The numerical methodology is briefly presented as follows. The convective fluxes are discretized using conservative skew-symmetric split-centered formulation. The viscous fluxes are discretized using the fourth order compact central differences scheme [14]. Time advancement is assessed by a standard explicit fourth-order Runge–Kutta algorithm. Turbulence is calculated using the large eddy simulation (LES) approach with a dynamic Smagorinsky–Lilly subgrid-scale model, which had been proven to be in very good agreement with experiments when solving flow orthogonally crossing a circular cylinder [15,16]. The subgrid-scale turbulent stress tensor is computed from

$$\tau_{ij} = -2\mu_t \bar{S}_{ij} + \frac{1}{3} \tau_{kk} \delta_{ij} \tag{4}$$

where  $\tau_{kk}$  is the isotropic part of the subgrid-scale stress.  $\bar{S}_{ij}$  is expressed as

$$\bar{S}_{ij} = \frac{1}{2} \left( \frac{\partial \bar{u}_i}{\partial x_j} + \frac{\partial \bar{u}_j}{\partial x_i} \right) \tag{5}$$

The turbulent viscosity is modeled by

$$\mu_t = \rho L_s^2 |\bar{S}|$$

where  $|\bar{S}| = \sqrt{2\bar{S}_{ij}\bar{S}_{ij}}$ ,  $L_s$  is computed using

$$L_s = \min(\kappa d, C_s V^{1/3})$$

where  $C_s$  is dynamically computed based on the information provided by the resolved scales of motion. To avoid numerical instability, in this calculation,  $C_s$  is clipped at 0 and 0.23.

First, flow orthogonally passing a circular cylinder at  $Re = 3900$  is taken as a benchmark to check the suitability and applicability of the LES approach in cross flow. Two flow characteristics are compared with the previous numerical and experimental data [16–21], which are respectively the downstream distribution of the streamwise velocity right away from the trailing edge and circumferential distribution of the base pressure coefficient, as shown in Figure 2a,b. They are in good agreement.

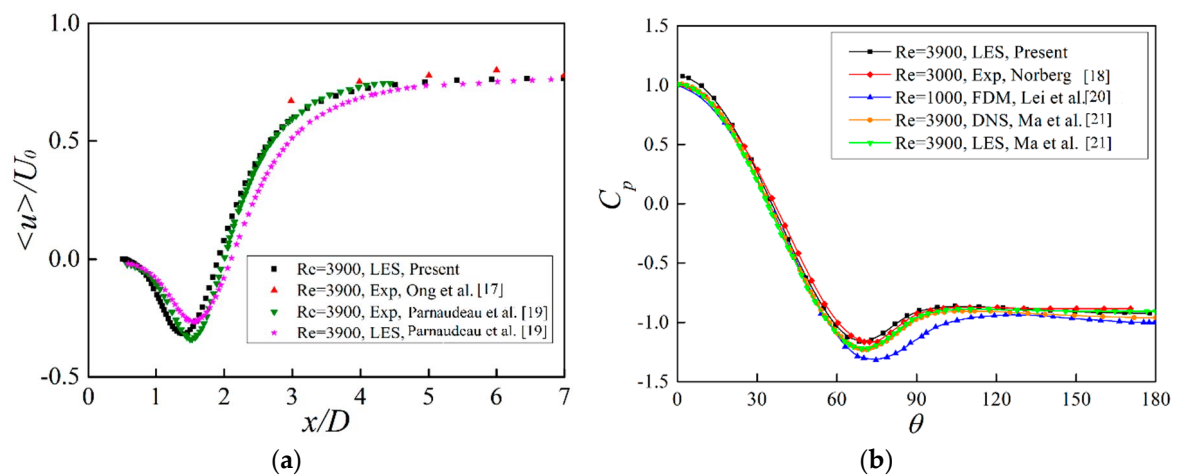


**Figure 2.** Verification of the numerical approach for flow orthogonally crossing a circular cylinder. (a) Streamwise velocity normalized by the free-stream velocity on the centerline in the wake; (b) pressure coefficient on the cylinder surface.

Second, mesh independence is established before numerical simulation. Incoming flow crossing a circular cylinder at  $\theta = 0^\circ$  and  $Re = 3900$  is still chosen as a benchmark to test the mesh independence. The meshing scheme in this study is taken as Case 2 in Table 1, with  $N_\theta \times N_z = 128 \times 54$  meshes on the cylinder surface and  $N_r = 110$  in the radial direction. Simulations of Case 1 with a coarser meshing and of Case 3 with a finer meshing are performed to check the mesh independence in the numerical simulation. Some typical flow parameters, such as drag coefficient, base pressure coefficient, and Strouhal number, are summarized from our computations and the results of Kravchenko et al. [16] large eddy simulations and the available experimental data, as shown in Table 1. It is found that the meshing scheme in Case 2 is in fairly good agreement with the experimental data and the results of the previous simulation. The final meshing scheme is set up as follows. The concentric annular region with a radius of  $4D$  around the cylinder axis is discretized with O-grid, and the other region is meshed with block structured H-grid. The mesh sizes at the adjoining area to the cylinder wall are determined by  $y^+ = 0.172 \times (\Delta y/D) \times Re^{0.9}$  [12], where  $\Delta y$  is the normal distance to the cylinder wall. The value of  $\Delta y$  is chosen to be  $3 \times 10^{-3}D$  to ensure  $y^+$  is less than 1. Moreover, at least two layers of nodes next to the cylinder wall are arranged within  $y^+ < 1$ . The maximal grid stretching factor is 1.02 for O-grid and 1.05 for block structured H-grid. The meshing scheme in the vicinity of the cylinder is shown in Figure 3.

**Table 1.** Mesh independence check for a single circular cylinder at  $\theta = 0^\circ$  and  $Re = 3900$ .

	Case 1	Case 2	Case 3	Experiments	Previous LES
$N_{total}$	387448	764964	1340496		
$N_\theta$	120	128	160		
$N_r$	84	110	114		
$N_z$	38	54	74		
$\bar{C}_D$	1.056542	1.046529	1.046528	$0.98 \pm 0.05$ [17]	1.04~1.07 [16]
$C_{pb}$	-0.99726	-0.96669	-0.96667	$0.90 \pm 0.05$ [18]	-0.98~-0.93 [16]
$Str$	0.216597	0.214875	0.214869	$0.215 \pm 0.005$ [22,23]	0.206~0.210 [16]

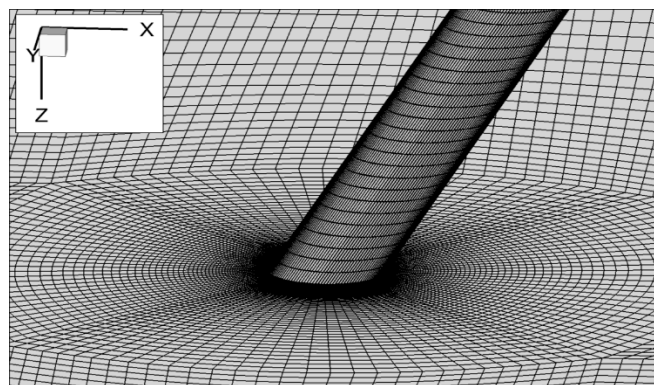


**Figure 3.** Meshing scheme in the vicinity of the cylinder.

### 3. Results and Discussion

The numerical simulations for flow crossing a yawed cylinder are carried out at three yaw angles ( $15^\circ$ ,  $30^\circ$ , and  $45^\circ$ ). Four flow characteristics are examined, i.e., vortex structure in the wake, streamline evolution fore-and-aft the cylinder and pressure distribution on the cylinder wall and frequency spectra of the local lift coefficient.

### 3.1. Wake Vortex Structure

The vortex structure is identified with  $Q$ -criterion (the second invariant  $Q$  from the velocity gradient tensor), which is favorable to capture a coherent vortex structure [24]. For a yawed cylinder, the incoming velocity is decomposed into two components, normal, and parallel to the cylinder axis. Considering the vortex production mechanism, the vortices in the wake are likely to result from two channels based on the wall boundary layer separation. One results from the separation of normal flow across a cylinder, hereinafter, named normal vortex, and the other comes out of the separation of axial flow through a cylinder, hereinafter, named axial vortex.

Under the periodic boundary condition on the two lateral end-plate walls, the vortex structure in the wake is shown in Figure 4a–c respectively at three yaw angles, viz.  $15^\circ$ ,  $30^\circ$ , and  $45^\circ$ . It is found that the vortex structure in the wake is independent of the yaw angle. Organized vortices are shed off from the cylinder into the wake in a quasi-two-dimensional manner and the series of rolling axes of the vortex structure are almost parallel to the cylinder axis (dotted line in Figure 4). This scenario of the vortex structure is of no prominent difference from a uniform flow normally crossing a circular cylinder.

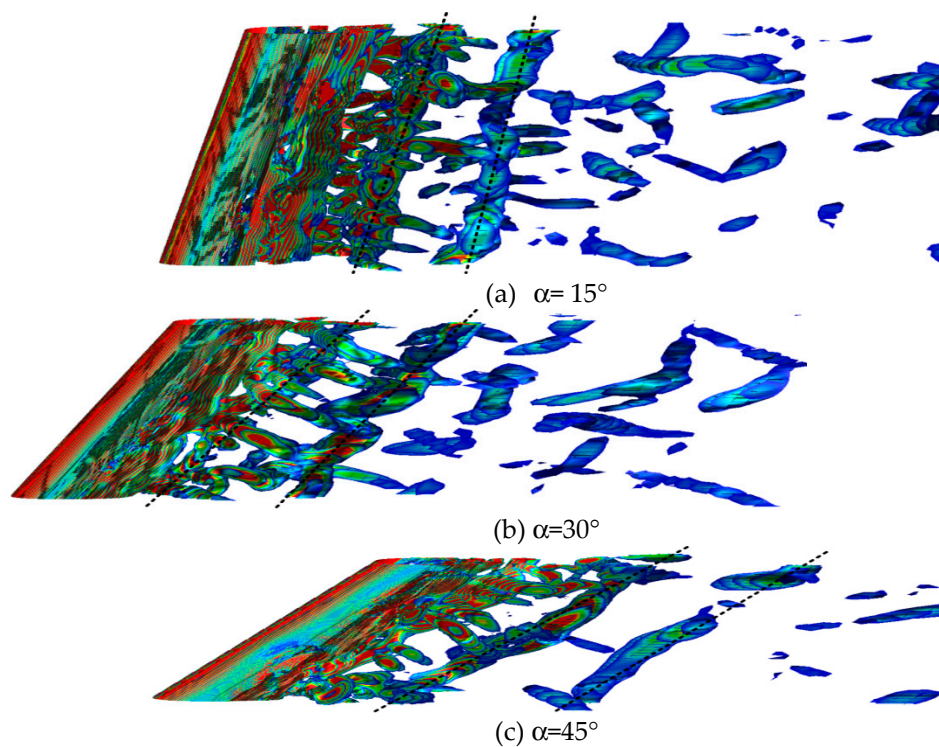


**Figure 4.** Vortex structure under periodic boundary condition on two end-plate walls.

Under the nonslip boundary condition on the two lateral endplate walls, the vortex structure in the wake, as shown in Figure 5a–c respectively at yaw angles of  $15^\circ$ ,  $30^\circ$ , and  $45^\circ$ , exhibits a dramatic difference from that under the periodic boundary condition. It is demonstrated that no organized Strouhal vortex is shed in the wake. The vortex structure in the wake is strongly axially varied and exhibits a tapering shape towards the tip end. At a large yaw angle, such as  $45^\circ$ , it even becomes a wedge shape lying on the tip end. Compared with the experiments [25], the numerical simulation is consistent with the experimental flow visualization.

Furthermore, the inspection of axial flow on the cylinder wall reveals that axial vortex appears in the wake. For clear demonstration, Figure 6 gives the axial vortex structure for a yaw angle of  $45^\circ$  (with a similar structure at the other two yaw angles of  $15^\circ$  and  $30^\circ$ ). The top view of  $Q$  contour, shown in Figure 6a, demonstrates that the free axial vortex in the wake is engendered from the separation of the axial boundary layer (herein, the normal vortex is screened). Furthermore, the side view of  $Q$

contour, shown in Figure 6b, reveals that two axial slender bands with high vorticity are symmetrically attached to the two flanks of the trailing edge.

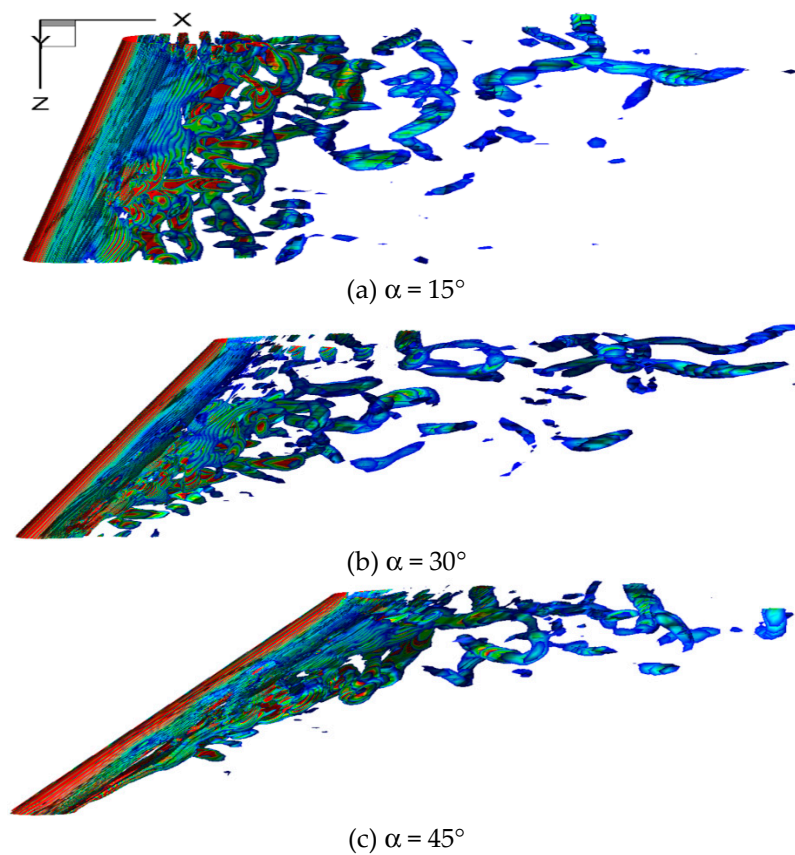


Figure 5. Vortex structure under nonslip boundary condition of two end-plate walls.

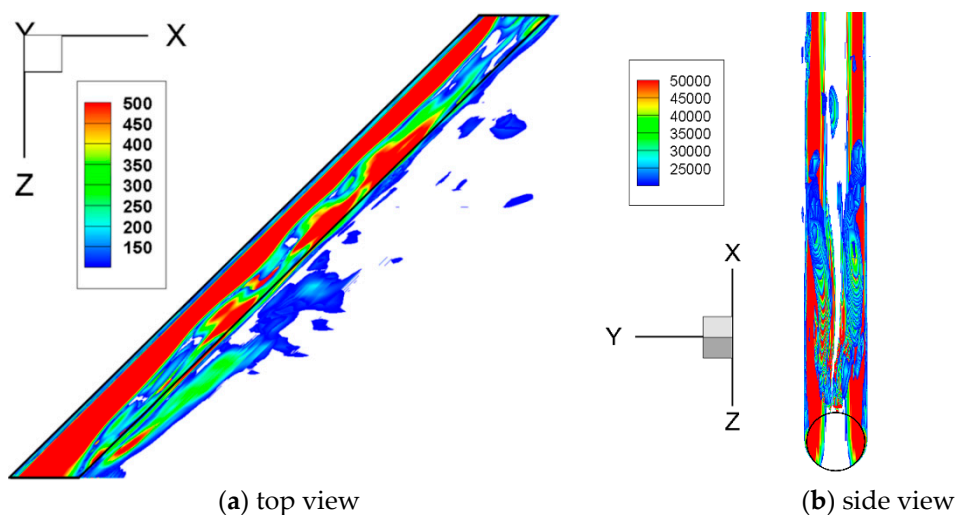


Figure 6. Axial vortices along the cylinder axis at  $\alpha = 45^\circ$ .

In addition, Figure 7 shows the whole vortex structure in the wake viewed in the axial direction, from which the relative geometrical relationship between the normal vortex and the axial vortices is illustrated. Two axial vortices are azimuthally symmetrically separated from the rear wall on the two sides of the trailing edge, whose separation points are azimuthally prior to the shedding point of the

normal vortex. In terms of the strength and size, the normal vortex is stronger and bigger than the axial vortices.

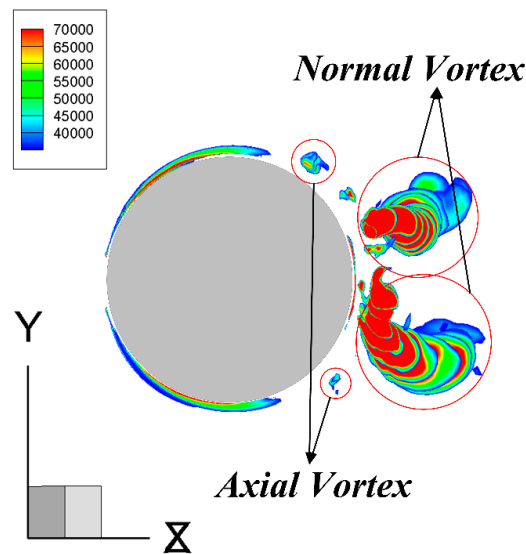


Figure 7. Comparisons of normal and axial vortices.

### 3.2. Streamlines

To discover the mechanism of the axial vortex separated from the rear wall of a cylinder, streamlines are depicted for both types of boundary condition on the two lateral endplate walls. The pattern of streamlines around a cylinder for the nonslip boundary condition is shown in Figure 8a–c respectively for yaw angles of  $15^\circ$ ,  $30^\circ$ , and  $45^\circ$ . As uniform streamlines approach the frontal wall of a cylinder, they begin to deflect tangentially towards the tip end of the cylinder. Then, they swerve to align normal to the cylinder and smoothly pass the frontal half of the cylinder wall. In the wake, the streamlines at the base side are pushed towards the tip side at the adjacent region to the cylinder, forming an axial flow attached to the rear surface of the cylinder along the cylinder axis. Up to the tip side, they are separated away from the cylinder at a certain point, the location of which is dependent on the yaw angle of the cylinder. The separated point is extended further towards the tip end with the increase of the yaw angle of the cylinder. Eventually, they return into the incoming direction before the cylinder. Finally, the flow pattern in the far region of the wake is transformed as follows: the streamlines on the tip side are becoming denser while the streamlines on the base side are becoming sparser. Thus, a strong shear flow including high vorticity is engendered between them.

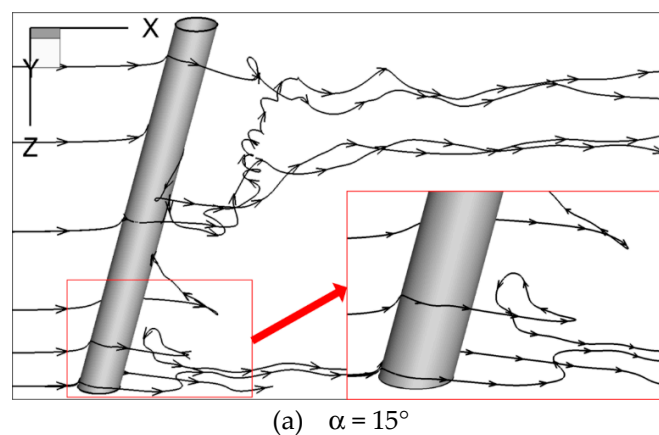
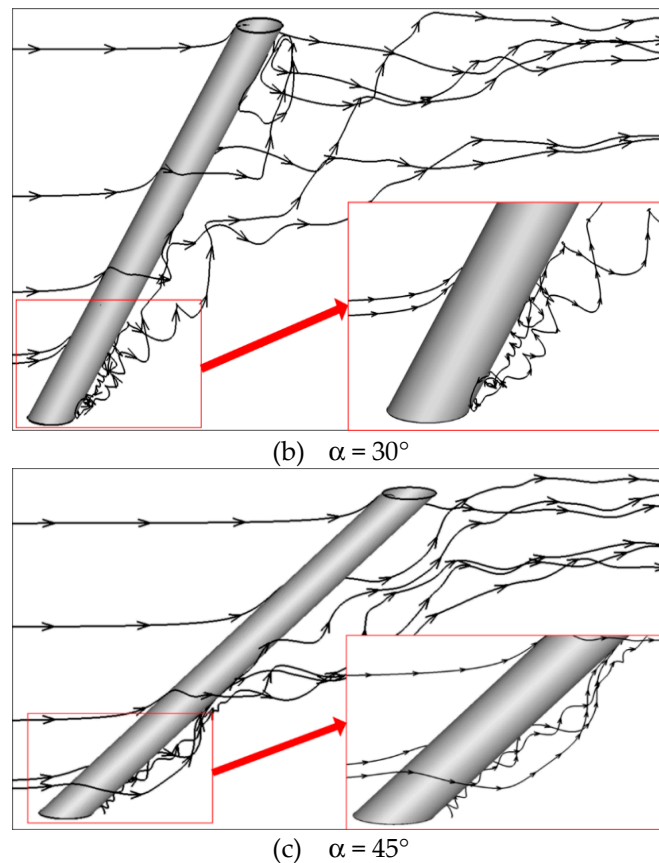


Figure 8. Cont.



**Figure 8.** Streamline development for three yaw angles under nonslip boundary condition.

Furthermore, at a large yaw angle such as  $30^\circ$  and  $45^\circ$ , a secondary wall-attached axial flow, besides the incoming streamlines, is originated around the trailing edge from the base end. It more tightly attaches to the wall of the cylinder. Finally, it is also separated from the wall and coalesces with the incoming flow.

Under the periodic boundary condition on the two lateral endplate walls, the streamline development crossing a cylinder is more regular than the above nonslip condition, as shown in Figure 9a–c. The incoming streamlines are deflected to align normal to the cylinder when approaching the cylinder wall. Moreover, when passing the upright ridge, they are deflected to the tip end under the advection of the primary axial velocity component, the trend of which is aggravated with the increase of yaw angle. At a yaw angle of  $45^\circ$ , they almost evolve into axial flow along the cylinder wall.

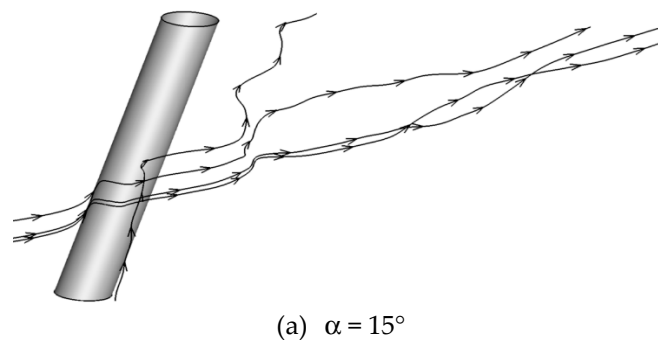


**Figure 9.** Cont.

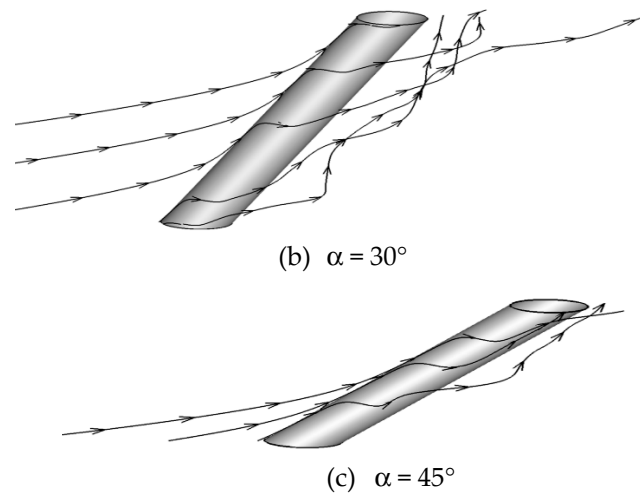


Figure 9. Streamline development for three yaw angles under periodic boundary condition.

### 3.3. Pressure Distribution on Cylinder Wall

To further investigate the intrinsic mechanism of the vortex structure in the wake, the pressure distribution on the cylinder wall is examined in two directions, viz.  $\theta$ - azimuthal and  $z'$ - axial directions, from numerical simulation results under the two types of boundary conditions on the two lateral end-plate walls. The surface pressure profiles are sampled from 9 circular circumferences of cylinder sections, which are equally spaced with one diameter space, as shown in Figure 10.

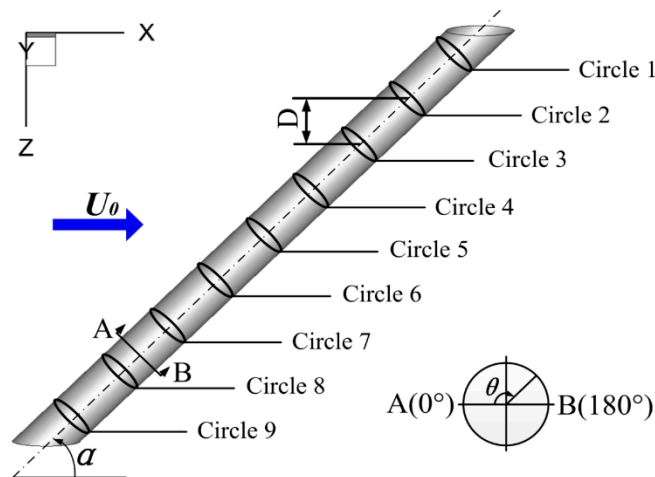


Figure 10. Sampling scheme of pressure distribution on cylinder wall.

#### 3.3.1. Non-Slip Boundary Condition

The pressure profiles on the nine circular circumferences at three yaw angles are shown respectively in Figure 11a–c. On the frontal wall up to about an azimuthal angle of  $60^\circ$ , the pressure distribution is of no axial variation. However, on most portion of the rear wall of the cylinder except the region around the trailing edge, the pressure is axially increased from the base end to the tip end, i.e., a positive axial pressure gradient is formed from the base side to the tip side, which increases with the yaw angle. Thus, separation of the above axial flow attached on the rear surface of the cylinder should be ascribed to the positive axial pressure gradient. In the region around the trailing edge, a convex pressure spike emerges at the base side and is more obvious for large yaw angles. The pressure spike engenders a positive pressure gradient in the base side and initiates the secondary axial flow around the trailing edge at the base end.

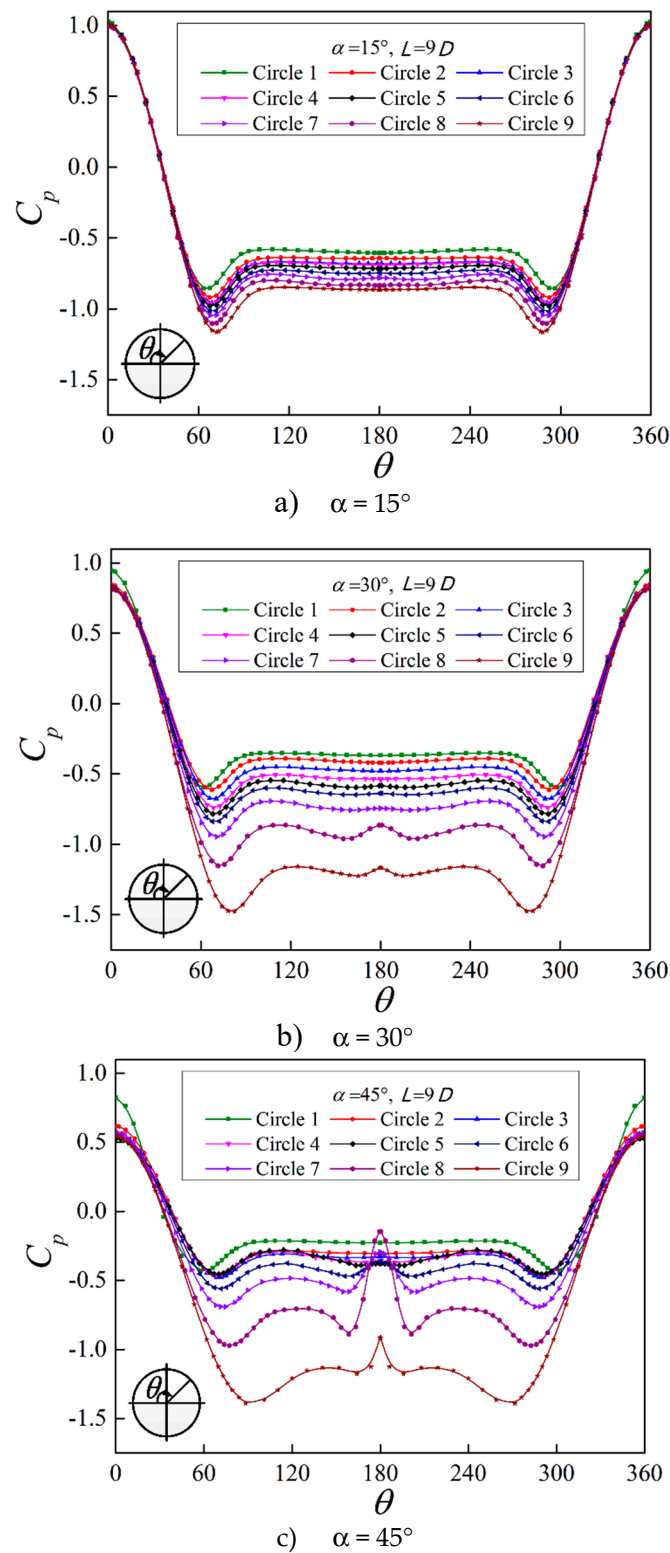


Figure 11. Pressure distribution on the cylinder wall under nonslip boundary condition.

### 3.3.2. Periodic Boundary Condition

Under the periodic boundary condition on the two end-plate walls, the pressure distribution on the cylinder wall manifests no axial variation. Figure 12 shows three pressure profiles, sampled respectively on the sectional circumferences in the base end, the midspan and the tip end, which are almost overlapped with each other. Therefore, no obvious secondary macroscale axial flow is induced,

the situation of which is the same as flow orthogonally crossing a cylinder. This is the reason why Strouhal vortex is regularly shed out of the cylinder wall as shown in Figure 4 and so the so-called IP is still applicable at a large yaw angle under periodic boundary conditions.

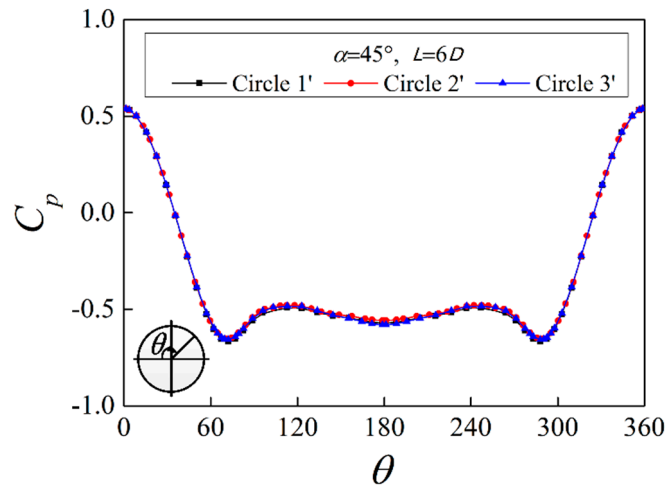


Figure 12. Pressure profiles under periodic boundary condition on the two end-plate walls at  $\alpha = 45^\circ$ .

### 3.4. Frequency Spectra of Local Lift Coefficient

To further explore the flow structure in the wake, the local lift coefficient is calculated from fluctuating pressure on the cylinder wall by integration. A yawed cylinder is virtually axially sliced into 9 segments with one diameter equal spacing. They are numbered in the same way as that for pressure distribution shown in Figure 10, viz. Segments 1 and 9 respectively correspond to the tip end and base end. The lift coefficient for each segment is analyzed in the frequency domain to capture its spectral characteristics. Figure 13 show the time histories of the lift coefficient in the midspan section sample at different yaw angles under the two boundary conditions.

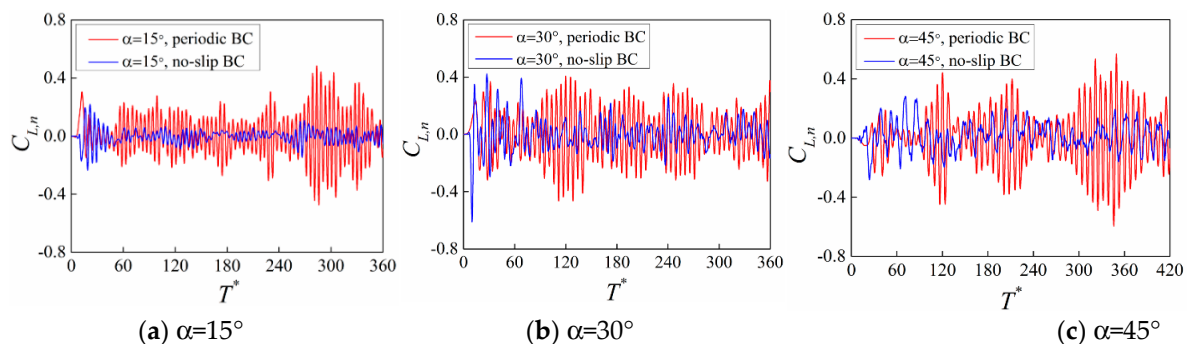


Figure 13. Time histories of lift coefficient for nonslip boundary condition and periodic boundary condition.

#### 3.4.1. Nonslip Boundary Condition

At a yaw angle of  $15^\circ$ , the power spectra of the lift coefficient for 9 segments are shown in Figure 14. For Segment 9 at the base end of the cylinder, the frequency spectra are broadband, which are evenly distributed from  $Str = 10^{-2}$  up to 0.3 with an energy level of approximately  $10^{-4}$ . Therefore, it convinces that no vortex is shed in the wake. In Segment 8, a narrowband peak appears at around  $Str = 0.2$ , the value of which is in agreement with that predicted by the independence principle ( $Str_{IP} = 0.2075$ ). From Segment 7 to Segment 4, two narrowband peaks appear respectively at  $Str = 0.025$  and 0.2. The energy level at  $Str = 0.2$  is in the order of  $10^{-3}$ , which is one order of magnitude higher than that of Segment 8. The low-frequency narrowband peak at  $Str = 0.025$  is likely to be associated with the separation of the secondary wall-attached axial flow because the location of Segment 4 corresponds to

the separation point of a secondary axial wall-attached flow as shown in Figure 8. For Segments 3 to 1, only the high-frequency peak consistent with that of the independence principle remains.

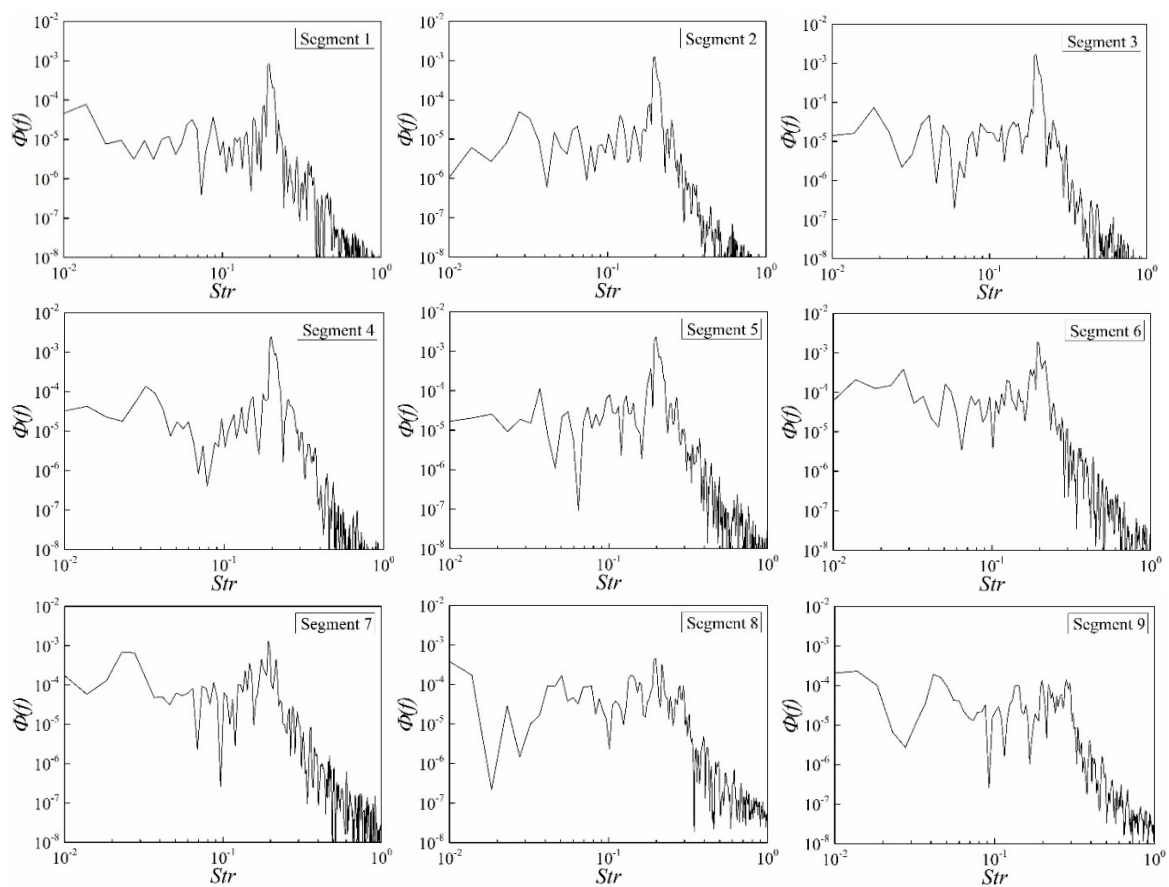


Figure 14. Power spectra of segmental lift coefficient at yaw angle of 15°.

At a yaw angle of 30° (as shown in Figure 15), the broadband spectra spanning from  $Str = 10^{-2}$  to 0.16 with an almost even energy distribution are extended from Segment 9 to Segment 5, where no vortex is shed in the wake. In Segment 4, two narrowband peaks appear. The higher one with  $Str = 0.16$  is consistent with the value of the independence principle, and the lower one with  $Str = 0.035$  is thought to be generated from the separation of the secondary wall-attached axial flow. For Segment 3 to 1 at the tip end, the narrowband corresponding to the value of the independent principle becomes prominent.

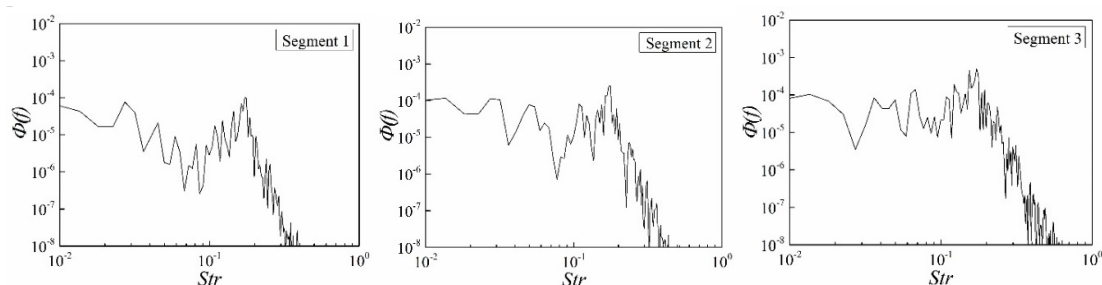


Figure 15. Cont.

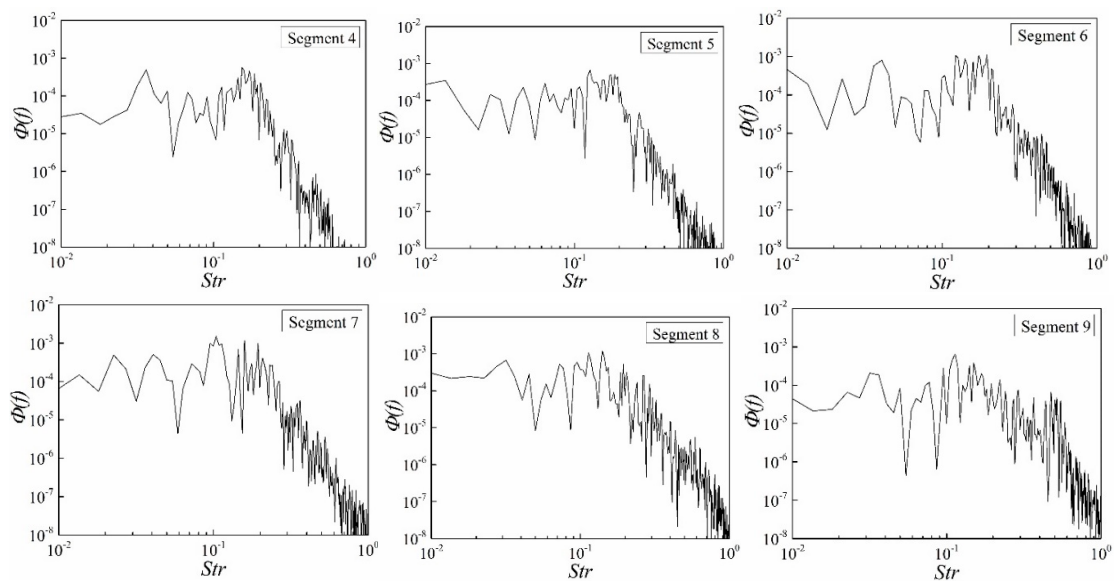


Figure 15. Power spectra of segmental lift coefficient at yaw angle of 30°.

When the yaw angle is increased to 45° (as shown in Figure 16), the most distinguished feature of the lift coefficient spectra is that the second harmonic of the primary mode appears for all 9 segments, the energy level of which is higher than that of the primary mode (approximately  $Str = 0.0968$  as predicted by the independence principle). The third peak appears in Segment 6 to 3, which should be ascribed to the contribution of the separation of the secondary wall-attached axial flow.

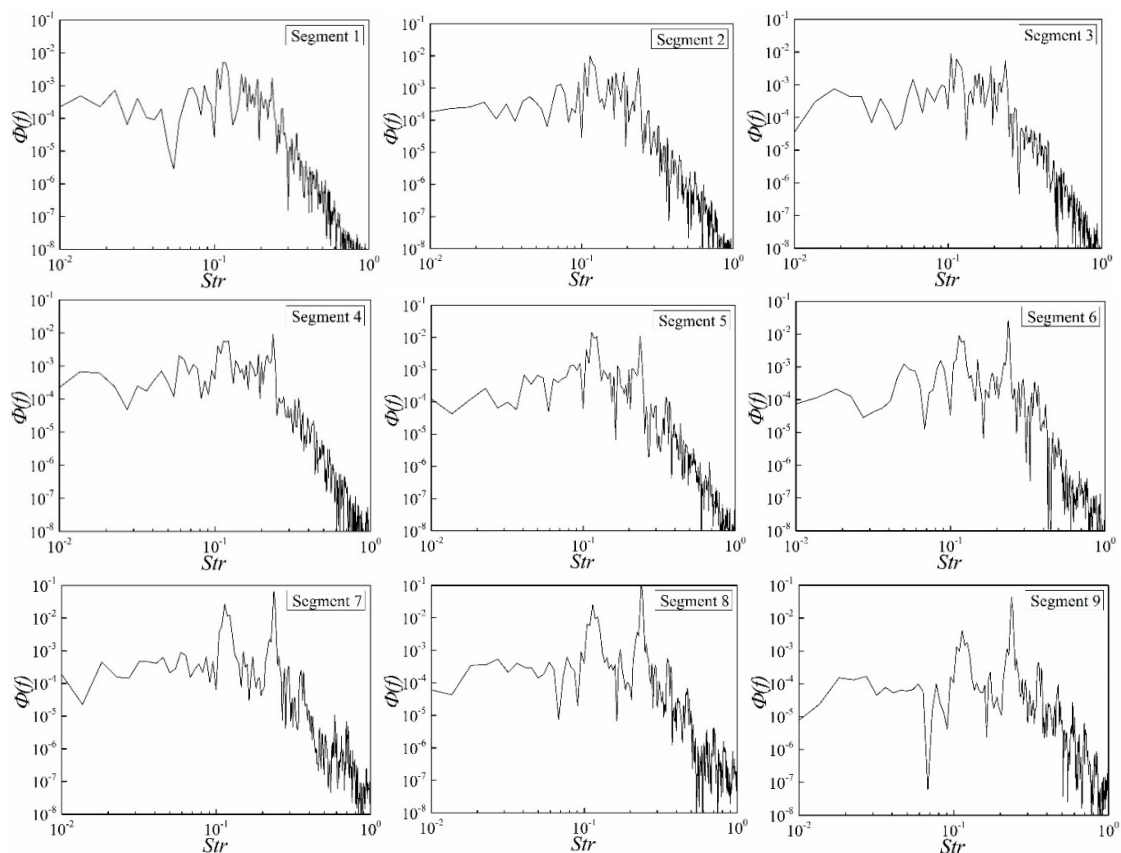


Figure 16. Power spectra of segmental lift coefficient at yaw angle of 45°.

### 3.4.2. Periodic Boundary Condition

The power spectra of the local lift coefficient show no axial dependence at periodic boundary condition on the two end plates, as shown in Figure 17a,b at yaw angles of  $30^\circ$  and  $45^\circ$ . They exhibit the same single peak, the value of which is consistent with the value of the independence principle. Recently, Wang et al. [26] explored the effect of yaw angle on the flow structure and cross-flow force around a circular cylinder using delayed detached eddy simulation. Their results also showed that the Strouhal number under the periodic condition at the two ends is well consistent with the value predicted by the IP.

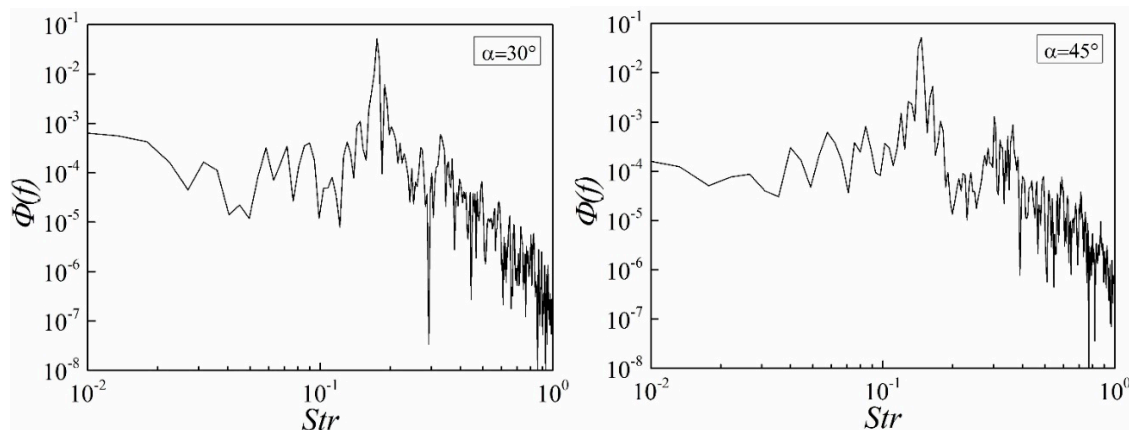


Figure 17. Power spectra of segmental lift coefficient at yaw angles of  $30^\circ$  and  $45^\circ$ .

## 4. Conclusions

The flow crossing a yawed circular cylinder at a subcritical Reynolds number of 3900 is numerically investigated using large eddy simulation (LES) at three yaw angles of  $15^\circ$ ,  $30^\circ$ , and  $45^\circ$ . The effect of the end-plate wall boundary condition on the vortex structure in the wake is investigated. Two boundary conditions of two end-plate walls are explored, respectively, viz. nonslip and periodic. The vortex structure in the wake and fore-and-aft streamline development are qualitatively examined. Moreover, the pressure profile on the cylinder wall and lift coefficient spectra of the segmental cylinder are quantitatively analyzed.

The numerical simulation results reveal that the boundary condition on the wall of two lateral end-plates is a decisive factor influencing the flow characteristics in the wake. Under the periodic boundary condition, the numerical simulations demonstrate that even at larger yaw angles (up to  $45^\circ$ ), the flow characteristics in the wake still hold a similar flow structure as flow normally crossing a circular cylinder. However, when the nonslip boundary condition is imposed on the two lateral end-plate walls, the flow behaviors in the wake become complicated and the vortex structure in the wake drastically deviates from regular Strouhal vortex shedding. The flow behaviors in the wake under the nonslip boundary condition can be concluded as follows.

- (1) Vortex structure: No organized Strouhal vortex is shed in the wake; the vortex structure in the wake exhibits a tapering shape towards the tip end. At a large yaw angle, such as  $45^\circ$ , it even becomes a wedge shape lying on the tip end.
- (2) Streamline: The incoming streamlines undergo several changes in direction when passing a yawed cylinder. In the wake, they are pushed towards the tip side and eventually separated away from the wall of the cylinder. The flow pattern is formed in the wake as the streamlines on the tip side are becoming denser while the streamlines on the base end are becoming sparser. Moreover, at a large yaw angle such as  $30^\circ$  and  $45^\circ$ , a secondary wall-attached axial flow, besides the incoming streamlines, is originated at the trailing edge from the base end, which is also separated from the wall and finally coalesces with the primary incoming flow.

- (3) Pressure distribution: On most portions of the rear wall of the cylinder except the region around the trailing edge, a positive axial pressure gradient is formed from the base side to the tip side, which contributes to the separation of the above axial flow attached on the rear surface of the cylinder. In the region around the trailing edge, a convex pressure spike at the base end initiates the secondary axial flow around the trailing edge.
- (4) Spectral power of local lift force: The power spectra analysis of the local lift coefficient shows that the frequency distribution is broadband in the base side while there are two peak frequencies in the tip side, where the larger one corresponds to the value predicted by the independent principle, and the smaller one is generated by the secondary axial flow separation from the rear wall of the cylinder. The authors should discuss the results and how they can be interpreted in the perspective of previous studies and the working hypotheses. The findings and their implications should be discussed in the broadest context possible. Future research directions may also be highlighted.

**Author Contributions:** Conceptualization, writing—review and editing, supervision, project administration, and funding acquisition are done by R.-Q.D. Methodology, software, validation, formal analysis, investigation, resources, data curation, writing—original draft preparation and visualization were done by H.L.

**Funding:** This research was funded by the National Natural Science Foundation of China (Grant No. 51779126).

**Conflicts of Interest:** The authors declare no conflict of interest.

## Nomenclature

$\bar{C}_D$	Mean drag coefficient, $\bar{C}_D = \int_0^{2\pi} C_p \cos \theta$
$C_{L,n}$	Lift coefficient normalized by $U_N$ , $C_{L,n} = 2F_L / (\rho D L U_N^2)$
$C_p$	Pressure coefficient, $C_p = 2(p - p_0) / (\rho U_0^2)$
$C_{pb}$	The time-averaged pressure coefficient at the backward stagnation point, $C_{pb} = (p_b - p_0) / (\rho U_0^2 / 2)$
$C_s$	Smagorinsky constant
$d$	Distance between mesh to the closest wall, m
$D$	Diameter of cylinder, m
$f$	Frequency of vortex shedding or boundary layer separation, Hz
$F_L$	Lift force on cylinder, N
$L$	Dimensional length of cylinder, m
$L_s$	Mixing length for subgrid scale, m
$N_r$	Mesh number in radial direction
$N_{total}$	Total mesh number in numerical simulation
$N_z$	Mesh number along an axis of a cylinder
$N_\theta$	Mesh number on the circumference of a cylinder
$\bar{p}$	Pressure, Pa
$p$	Dimensionless pressure
$p_0$	Dimensionless pressure of incoming flow
$p_b$	Dimensionless base pressure at the backward stagnation point
$Re$	Reynolds number, $Re = U_0 D / \nu$
$\bar{S}_{ij}$	Rate-of-strain tensor
$Str$	Strouhal number, $Str = fD / U_0$
$\bar{t}$	Time, s
$t$	Dimensionless time
$u$	Dimensionless velocity vector
$U_0$	Velocity of incoming flow, m/s
$U_N$	Normal component of velocity of incoming flow, m/s
$\langle u \rangle / U_0$	Time-averaged streamwise velocity on the centerline in the wake of a circular cylinder
$V$	Volume of computational cell, m <sup>3</sup>
$\bar{x}$	Coordinate, m

$x$	Dimensionless coordinate
$\alpha$	Cylinder yaw angle, deg
$\kappa$	Von Karman constant
$\mu_t$	Subgrid-scale turbulent viscosity
$\tau_{ij}$	Subgrid-scale turbulent stress tensor
$\varphi(f)$	Spectra power density

## References

1. Hoerner, S.F. *Fluid-Dynamic Drag: Practical Information on Aerodynamic Drag and Hydrodynamic Resistance*; SF Hoerner: Midland Park, NJ, USA, 1965.
2. Selby, G.V. Applicability of the independence principle to subsonic turbulent flow over a swept rearward-facing step. *AIAA J.* **1983**, *21*, 1603–1604. [[CrossRef](#)]
3. Hayashi, T.; Kawamura, T. Non-uniformity in a flow around a yawed circular cylinder. *Flow Meas. Instrum.* **1995**, *6*, 33–39. [[CrossRef](#)]
4. Zhao, M.; Cheng, L.; Zhou, T. Direct numerical simulation of three-dimensional flow past a yawed circular cylinder of infinite length. *J. Fluids Struct.* **2009**, *25*, 831–847. [[CrossRef](#)]
5. Hogan, J.D.; Hall, J.W. The Spanwise Dependence of Vortex-Shedding from Yawed Circular Cylinders. *J. Press. Vessel Technol.* **2010**, *132*. [[CrossRef](#)]
6. Zeinoddini, M.; Farhangmehr, A.; Seif, M.S.; Zandi, A.P. Cross-flow vortex induced vibrations of inclined helically straked circular cylinders: An experimental study. *J. Fluids Struct.* **2015**, *59*, 178–201. [[CrossRef](#)]
7. Pierson, J.-L.; Hammouti, A.; Franck, A.; Wachs, A. Flow Past a Yawed Cylinder of Finite Length Using a Fictitious Domain Method. In Proceedings of the 10th International Conference on Computational Fluid Dynamics in the Oil & Gas, Metallurgical and Process Industries, Trondheim, Norway, 30 May–1 June 2017.
8. Ramberg, S.E. The effects of yaw and finite length upon the vortex wakes of stationary and vibrating circular cylinders. *J. Fluid Mech.* **1983**, *128*, 81–107. [[CrossRef](#)]
9. Matsumoto, M. Vortex shedding of bluff bodies: A review. *J. Fluids Struct.* **1999**, *13*, 791–811. [[CrossRef](#)]
10. Matsumoto, M.; Yagi, T.; Shigemura, Y.; Tsushima, D. Vortex-induced cable vibration of cable-stayed bridges at high reduced wind velocity. *J. Wind Eng. Ind. Aerodyn.* **2001**, *89*, 633–647. [[CrossRef](#)]
11. Matsumoto, M. The role of axial flow in near wake on the cross-flow vibration of the inclined cable of cable-stayed bridges. In Proceedings of the ASME 2010 3rd Joint US-European Fluids Engineering Summer Meeting collocated with 8th International Conference on Nanochannels, Microchannels, and Minichannels, Montreal, QC, Canada, 1–5 August 2010; pp. 35–43. [[CrossRef](#)]
12. Schlichting, H. *Boundary-Layer Theory*, 8th ed.; Springer: Berlin, Germany, 2000.
13. Batchelor, G.K. *An Introduction to Fluid Dynamics*; Cambridge University Press: Cambridge, UK, 2000. [[CrossRef](#)]
14. Shadloo, M.S.; Hadjadj, A.; Chaudhuri, A.; Ben-Nasr, O. Large-eddy simulation of a spatially-evolving supersonic turbulent boundary layer at  $M_\infty = 2$ . *Eur. J. Mech. B Fluids* **2018**, *67*, 185–197. [[CrossRef](#)]
15. Breuer, M. Numerical and modeling influences on large eddy simulations for the flow past a circular cylinder. *Int. J. Heat Fluid Flow* **1998**, *19*, 512–521. [[CrossRef](#)]
16. Kravchenko, A.G.; Moin, P. Numerical studies of flow over a circular cylinder at  $Re_D = 3900$ . *Phys. Fluids* **2000**, *12*, 403–417. [[CrossRef](#)]
17. Ong, L.; Wallace, J. The velocity field of the turbulent very near wake of a circular cylinder. *Exp. Fluids* **1996**, *20*, 441–453. [[CrossRef](#)]
18. Norberg, C. *Effects of Reynolds Number and Low-Intensity Freestream Turbulence on the Flow Around a Circular Cylinder*; Publikation Nr 87/2; Chalmers University: Goteborg, Sweden, 1987.
19. Parnaudeau, P.; Carlier, J.; Heitz, D.; Lamballais, E. Experimental and numerical studies of the flow over a circular cylinder at Reynolds number 3900. *Phys. Fluids* **2008**, *20*, 085101. [[CrossRef](#)]
20. Lei, C.; Cheng, L.; Kavanagh, K. Spanwise length effects on three-dimensional modelling of flow over a circular cylinder. *Comput. Methods Appl. Mech. Eng.* **2001**, *190*, 2909–2923. [[CrossRef](#)]
21. Ma, X.; Karamanos, G.S.; Karniadakis, G.E. Dynamics and low-dimensionality of a turbulent near wake. *J. Fluid Mech.* **2000**, *410*, 29–65. [[CrossRef](#)]

22. Cardell, G.S. Flow Past a Circular Cylinder with a Permeable Wake Splitter Plate. Ph.D. Thesis, California Institute of Technology, Pasadena, CA, USA, 1993.
23. Roshko, A. On the Development of Turbulent Wakes from Vortex Streets. Ph.D. Thesis, California Institute of Technology, Pasadena, CA, USA, 1952.
24. Jeong, J.; Hussain, F. On the identification of a vortex. *J. Fluid Mech.* **1995**, *285*, 69–94. [[CrossRef](#)]
25. Matsuzaki, K.; Shingai, M.; Haramoto, Y.; Munekata, M.; Ohba, H. Visualization of three-dimensional flow structures in the wake of an inclined circular cylinder. *J. Vis.* **2004**, *7*, 309–316. [[CrossRef](#)]
26. Wang, R.; Cheng, S.; Ting, D.S.K. Effect of yaw angle on flow structure and cross-flow force around a circular cylinder. *Phys. Fluids* **2019**, *31*, 014107. [[CrossRef](#)]



© 2019 by the authors. Licensee MDPI, Basel, Switzerland. This article is an open access article distributed under the terms and conditions of the Creative Commons Attribution (CC BY) license (<http://creativecommons.org/licenses/by/4.0/>).